Magnetic properties of single crystalline itinerant ferromagnet $AlFe_2B_2$

Tej N. Lamichhane,[1,2,*] Li Xiang,[1,2] Qisheng Lin,[1] Tribhuwan Pandey,[3] David S. Parker,[3] Tae-Hoon Kim,[1] Lin Zhou,[1] Matthew J. Kramer,[1] Sergey L. Bud'ko,[1,2] and Paul C. Canfield[1,2]

[1]*Ames Laboratory, U.S. DOE, Ames, Iowa 50011, USA*

[2]*Department of Physics and Astronomy, Iowa State University, Ames, Iowa 50011, USA*

[3]*Materials Science and Technology Division, Oak Ridge National Laboratory, Oak Ridge, Tennessee 37831, USA*

(Received 15 May 2018; published 20 August 2018)

Single crystals of $AlFe_2B_2$ have been grown using the self-flux growth method, and then we measured the structural properties, temperature- and field-dependent magnetization, and temperature-dependent electrical resistivity at ambient as well as high pressure. The Curie temperature of $AlFe_2B_2$ is determined to be 274 K. The measured saturation magnetization and the effective moment for the paramagnetic Fe ion indicate the itinerant nature of the magnetism with a Rhode-Wohlfarth ratio $\frac{M_C}{M_{sat}} \approx 1.14$. Temperature-dependent resistivity measurements under hydrostatic pressure show that transition temperature T_C is suppressed down to 255 K for $p = 2.24$ GPa pressure with a suppression rate of ~ -8.9 K/GPa. The anisotropy fields and magnetocrystalline anisotropy constants are in reasonable agreement with density functional theory calculations.

DOI: 10.1103/PhysRevMaterials.2.084408

I. INTRODUCTION

In recent years, $AlFe_2B_2$ has attracted a growing research interest as a rare-earth free ferromagnet that might have potential as a magnetocaloric material [1,2]. It is a layered material that has been identified as an itinerant ferromagnet [3]. $AlFe_2B_2$ was first reported by Jeitschko [4] and independently by Kuz'ma and Chaban [5]. $AlFe_2B_2$ crystallizes in an orthorhombic structure with space group *Cmmm* (Mn_2AlB_2 structure type). The Al atoms located in the 2*a* crystallographic position (0,0,0) form a plane that alternately stacks with Fe-B slabs formed by Fe atoms located at $4j$(0, 0.3554, 0.5) and B atoms located at $4i$ (0,0.1987,0) positions [6]. A unit cell for $AlFe_2B_2$ is shown in Fig. 1(a). $AlMn_2B_2$ and $AlCr_2B_2$ are the other two known isostructural transition-metal compounds. The magnetic nature of $AlMn_2B_2$ and $AlCr_2B_2$ is not clearly understood [7]. Among these three members, only $AlFe_2B_2$ is ferromagnetic; however, the reported magnetic parameters for $AlFe_2B_2$ show a lot of variation [1–3,6,8]. A good summary of all of these variations was presented recently in tabular form in the literature [9].

For example, the Curie temperature of this material is reported to fall within a window of 274–320 K depending upon the synthesis route. Initial work indicates that the Curie temperature of $AlFe_2B_2$ was 320 K [3]. The Curie temperature of Ga-flux-grown $AlFe_2B_2$ was reported to be 307 K, and for arc-melted polycrystalline samples it was reported to be 282 K [1]. The Curie temperature for annealed, melt-spun ribbons was reported to be 312 K [6]. A Mössbauer study on arc-melted and annealed samples reported a Curie temperature of 300 K [2]. At the lower limit, the Curie temperature of spark plasma sintered $AlFe_2B_2$ was reported to be 274 K [8]. The reported saturation magnetic moment also manifests up to a 25% variation from the theoretically predicted saturation moment of $1.25\mu_B$/Fe. The first reported saturation magnetization and effective moment values for $AlFe_2B_2$ were $1.9(2)\mu_B$/f.u. at 4.2 K and $4.8\mu_B$/Fe, respectively [3]. Similarly, Du *et al.* reported a saturation magnetization moment of $1.32\mu_B$/Fe at 5 K [10]. Recently, Tan *et al.* reported a saturation magnetization of $1.15\mu_B$/Fe and $1.03\mu_B$/Fe for before and after the HCl etching of an arc-melted sample [1]. The lower saturation moment, after the acid etching, suggested either the inclusion of Fe-rich magnetic impurities in the sample or degradation of the sample with acid etching. Recently, a study pointed out that the content of impurity phases decreases with an excess of Al in the as-cast alloy and by annealing [11]. The main reason for the variation in the reported magnetic parameters is the difficulty in preparing pure single-crystal, single-phase $AlFe_2B_2$ samples. To this end, detailed measurements on single-phase, single crystalline samples will provide unambiguous magnetic parameters and general insight into $AlFe_2B_2$.

In this work, we investigated the magnetic and transport properties of self-flux-grown single crystalline $AlFe_2B_2$. We report single crystalline structural, magnetic, and transport properties of $AlFe_2B_2$. We find that $AlFe_2B_2$ is an itinerant ferromagnet with $\frac{M_C}{M_{sat}} \approx 1.14$ and the Curie temperature is initially linearly suppressed with hydrostatic pressure at a rate of $\frac{dT_C}{dp} \sim -8.9$ K/GPa. The magnetic anisotropy fields of $AlFe_2B_2$ are $\sim$1 T along the [010] and $\sim$5 T along the [001] direction. The first magnetocrystalline anisotropic constants (K_1's) at base temperature are determined to be $K_{010} \approx 0.23$ MJ/m^3 and $K_{001} \approx 1.8$ MJ/m^3 along the [010] and [001] directions, respectively. (The subscript 1 is dropped for simplicity.)

II. EXPERIMENTAL DETAILS

A. Crystal growth

Single crystalline samples were prepared using a self-flux-growth technique [12]. First we confirmed that our initial stoichiometry $Al_{50}Fe_{30}B_{20}$ was a single phase liquid at 1200 °C.

*Corresponding author: tejl@iastate.edu

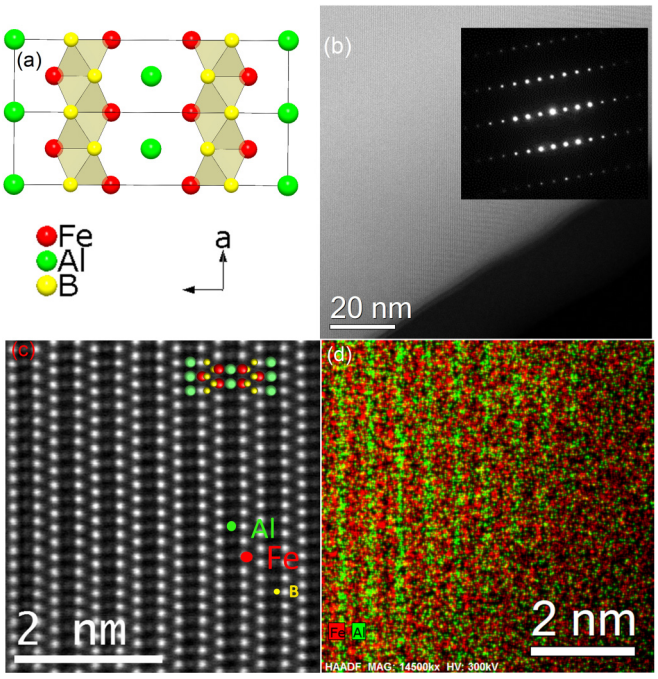

FIG. 1. (a) $AlFe_2B_2$ unit cell. (b) The HAADF STEM image shows the uniform chemistry of the $AlFe_2B_2$ crystal. The inset is a corresponding selected-area electron diffraction pattern. (c) High-resolution HAADF STEM image of $AlFe_2B_2$ taken along the [101] zone axis along with a projection of a unit cell represented with Fe (red), Al (green), and B (yellow) spheres. The structural pattern of Al and FeB slab layers is also visible in the unit cell shown in (a). (d) EDS elemental mapping without taking into account of the B scattering effect, where green stripes are Al distributions and red stripes are Fe distributions.

Starting composition $Al_{50}Fe_{30}B_{20}$ with elemental Al (Alfa Aesar, 99.999%), Fe (Alfa Aesar, 99.99%), and B (Alfa Aesar, 99.99%) was arc-melted under an Ar atmosphere at least four times. The ingot was then crushed with a metal cutter and put in a fritted alumina crucible set [13] under the partial pressure of Ar inside an amorphous SiO_2 jacket for the purpose of flux growth. The growth ampoule was heated to 1200 °C over 2–4 h and allowed to homogenize for 2 h. The ampoule was then placed in a centrifuge, and all liquid was forced to the catch side of the crucible. Given that all of the melt was collected in the catch crucible, this confirms that $Al_{50}Fe_{30}B_{20}$ is liquid at 1200 °C.

Knowing that the arc-melted $Al_{50}Fe_{30}B_{20}$ composition exists as a homogeneous melt at 1200 °C, the cooling profile was optimized as follows. The homogeneous melt at 1200 °C was cooled down to 1180 °C over 1 h and slowly cooled down to 1080 °C over 30 h, at which point the crucible limited, platelike crystals were separated from the remaining flux using a centrifuge. The large platelike crystals had some $Al_{13}Fe_4$ impurity phase on their surfaces that was removed with dilute HCl etching [8]. The as-grown single crystals are shown in the insets of Fig. 2(a) .

B. Characterization and physical property measurements

The crystal structure of $AlFe_2B_2$ was characterized with both single-crystal x-ray diffraction (XRD) and powder XRD. The single-crystal XRD data were collected within a 4°–29° angle value of 2θ using a Bruker Smart APEX II diffractometer with a graphite-monochromatized Mo $K\alpha$ radiation source ($\lambda = 0.710\,73$ Å). The powder-diffraction data were collected using a Rigaku MiniFlex II diffractometer with Cu $K\alpha$ radiation. The acid-etched $AlFe_2B_2$ crystals were ground to a fine powder and spread over a zero background, Si-wafer sample holder with the help of a thin film of Dow Corning high vacuum grease. The diffraction intensity data were collected within a 2θ interval of 5°–100° with a fixed dwelling time of 3 s and a step size of 0.01°.

The as-grown single crystalline sample was examined with transmission electron microscopy to obtain high-angle annular-dark-field (HAADF) scanning transmission electron microscopy (STEM) images, a corresponding selected-area electron diffraction pattern, and a high-resolution HAADF STEM image of $AlFe_2B_2$ taken under the [101] zone axis.

The anisotropic magnetic measurements were carried out in a Quantum Design Magnetic Property Measurement System (MPMS) for $2 \leqslant T \leqslant 300$ K and a Versalab Vibrating Sample Magnetometer (VSM) for $50 \leqslant T \leqslant 700$ K.

The temperature-dependent resistivity of $AlFe_2B_2$ was measured in a standard four-contact configuration, with contacts prepared using silver epoxy. The excitation current was along the crystallographic a axis. ac resistivity measurements were performed in a Quantum Design Physical Property Measurement System (PPMS) using 1 mA, 17 Hz excitation, with cooling at a rate of 0.25 K/min. A Be-Cu/Ni-Cr-Al hybrid piston-cylinder cell similar to the one described in Ref. [14] was used to apply pressure. Pressure values at the transition temperature T_C were estimated by linear interpolation between the room-temperature pressure $p_{300\,\mathrm{K}}$ and low-temperature pressure $p_{T\leqslant 90\,\mathrm{K}}$ values [15,16]. $p_{300\,\mathrm{K}}$ values were inferred from the 300 K resistivity ratio $\rho(p)/\rho(0\,\mathrm{GPa})$ of lead [17], and $p_{T\leqslant 90\,\mathrm{K}}$ values were inferred from the $T_c(p)$ of lead [18]. Good hydrostatic conditions were achieved by using a 4:6 mixture of light mineral oil:*n*-pentane as a pressure medium; this mixture solidifies at room temperature in the range 3–4 GPa, i.e., well above our maximum pressure [14,16,19].

III. EXPERIMENTAL RESULTS

A. Structural characterization

The HAADF STEM image along with a selected area diffraction pattern in the inset and a high-resolution HAADF STEM image of $AlFe_2B_2$ taken under the [101] zone axis and EDS Al-Fe elemental mapping are presented in panels (b), (c), and (d) of Fig. 1. Taken together, they strongly suggest the uniform chemical composition of $AlFe_2B_2$ throughout the sample.

The crystallographic solution and parameter refinement on the single crystalline XRD data were performed using the SHELXTL program package [20]. The Rietveld refined single crystalline data are presented in Tables I and II. Using the atomic coordinates from the crystallographic information file obtained from single-crystal XRD data, powder XRD data were Rietveld-refined with $R_P = 0.1$ using a general structure analysis system [21] [Fig. 2(a)]. The lattice parameters from the powder XRD are $a = 2.920(4)$ Å, $b = 11.026(4)$ Å, and

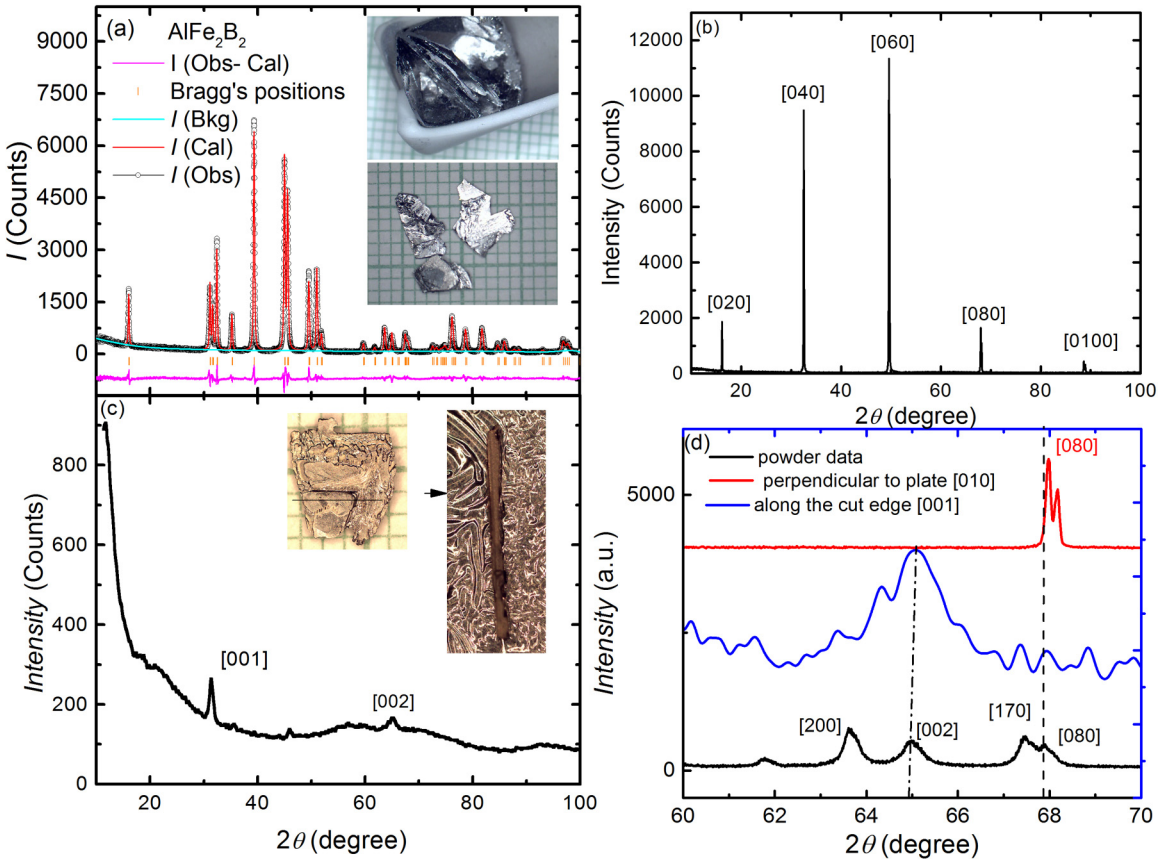

FIG. 2. (a) Powder XRD for $AlFe_2B_2$. I(Obs), I(Cal), and I(Bkg) stand for experimental powder diffraction, Rietveld refined, and instrumental background data. The green vertical lines represent the Bragg reflection peaks, and I(Obs-Cal) is the differential intensity between I(Obs) and I(Cal). The upper inset shows the crucible limited growth nature of $AlFe_2B_2$. The lower inset shows the pieces of as-grown platelike crystals. (b) Monochromatic XRD pattern from the plate surface of $AlFe_2B_2$. (c) Monochromatic XRD pattern from cut surface [001] collected using Bragg-Brentano geometry. The left inset shows the as-grown $AlFe_2B_2$ crystal. The right inset is the photograph of the cut section of the crystal parallel to the (001) plane. The middle unidentified peak might be due to a differently oriented shard of cut $AlFe_2B_2$ crystal. (d) Comparison of the monochromatic surface XRD patterns from (b) and (c) with a powder XRD pattern from (a) within an extended 2θ range of 60°–70° to illustrate the identification scheme of the crystallographic orientation.

$c = 2.866(7)$ Å, which are in reasonable agreement with the single-crystal data analysis values.

To confirm the crystallographic orientation of the $AlFe_2B_2$ crystals, monochromatic Cu $K\alpha$ XRD data were collected from the flat surface of the crystals and found to be in the {020} family, as shown in Fig. 2(b), i.e., the [010] direction is perpendicular to the plate. However, finding a thick enough, flat, as-grown facet with the [100] and [001] directions was made difficult by the thin, sheetlike morphology of the sample and its crucible limited growth nature. A [001] facet was cut out of a large crucible limited crystal as shown in the inset of Fig. 2(c). The monochromatic Cu $K\alpha$ XRD pattern scattered from the cut surface confirms the [001] direction displaying the [001] and [002] peaks [Fig. 2(c)]. To better illustrate the crystallographic orientations, powder XRD, and monochromatic surface XRD, patterns from the plate surface and the cut edge are plotted together in Fig. 2(d). This plot clearly identifies that the direction perpendicular to the plate is [010] and the cut edge surface is (001). A slight displacement of the surface XRD peaks is the result of the sample height in the Bragg-Brentano geometry. The splitting of the [080] peak is observed by distinction of Cu $K\alpha$ satellite XRD patterns usually observed at high diffraction angles.

IV. MAGNETIC PROPERTIES

The anisotropic magnetization data were measured using a sample with known crystallographic orientation. The temperature-dependent magnetization $M(T)$ data along the [100] axis are presented in Fig. 3(a). Both the zero-field-cooled warming (ZFCW) and field-cooled (FC) $M(T)$ data are almost overlapping for a 0.01 T applied field. The $M(T)$ data suggest a Curie temperature (T_C) of ~275 K using an inflection point of $M(T)$ data as a criterion. This value will be determined more precisely below to be $T_C = 274$ K using easy-axis $M(H)$ isotherms around the Curie temperature.

Figure 3(b) shows the anisotropic, field-dependent magnetization at 2 K. The saturation magnetization (M_{sat}) at 2 K is determined to be $2.40\mu_B$/f.u., i.e., roughly half of the bulk bcc Fe moment. The anisotropic $M(H)$ data at 2 K show that [100] is the easy axis, the [010] axis is a harder axis with an anisotropy field of ≈1 T, and [001] is the hardest axis of magnetization with an anisotropy field of ≈5 T. A

TABLE I. Crystal data and structure refinement for $AlFe_2B_2$.

Empirical formula	$AlFe_2B_2$
Formula weight	160.3
Temperature	293(2) K
Wavelength	0.71073 Å
Crystal system, space group	Orthorhombic, *Cmmm*
Unit-cell dimensions	$a = 2.9168(6)$ Å
	$b = 11.033(2)$ Å
	$c = 2.8660(6)$ Å
Volume	92.23(3) 10^3 Å^3
Z, calculated density	2, 5.75 g/cm^3
Absorption coefficient	31.321 mm^{-1}
$F(000)$	300
θ range (deg)	3.693–29.003
Limiting indices	$-3 \leqslant h \leqslant 3$
	$-14 \leqslant k \leqslant 14$
	$-3 \leqslant l \leqslant 3$
Reflections collected	402
Independent reflections	7[R(int) = 0.0329]
Absorption correction	multiscan, empirical
Refinement method	Full-matrix least-squares on F^2
Data/restraints/parameters	74/0/12
Goodness-of-fit on F^2	1.193
Final R indices [$I > 2\sigma(I)$]	$R1 = 0.0181$, $wR2 = 0.0467$
R indices (all data)	$R1 = 0.0180$, $wR2 = 0.0467$
Largest difference peak and hole	0.679 and −0.880 e Å^{-3}

Sucksmith-Thompson plot [22], using $M(H)$ data along [001], is shown in Fig. 3(c). The inset to Fig. 3(c) shows data for H along [010]. In a Sucksmith-Thompson plot, the Y intercept of the linear fit of hard axis $\frac{H_{\rm int}}{M}$ versus M^2 isotherm provides the magnetocrystalline anisotropy constant (intercept $= \frac{2K_1}{M_S{}^2}$, M_S being saturation magnetization at 2 K) of the material. From these plots, we determined $K_{010} = 0.23$ MJ/m^3 and $K_{001} = 1.78$ MJ/m^3 respectively.

Given that $AlFe_2B_2$ has $T_C \sim$ room temperature, and is formed from earth abundant elements, it is logical to examine it as a possible magnetocaloric material. The easy-axis [100] $M(H)$ isotherms around the Curie temperature [shown for the Arrott plot in Fig. 3(d)] were used to estimate the magnetocaloric property for $AlFe_2B_2$ in terms of entropy change using the following equation [1,23]:

$$\Delta S\left(\frac{T_1+T_2}{2}, \Delta H\right) \approx \frac{\mu_0}{T_2-T_1}\int_{H_i}^{H_f} M(T_2,H) - M(T_1,H)dH, \qquad (1)$$

TABLE II. Atomic coordinates and equivalent isotropic displacement parameters (A^2) for $AlFe_2B_2$. $U_{\rm eq}$ is defined as one-third of the trace of the orthogonalized U_{ij} tensor.

Atom	Wyckoff site	x	y	z	$U_{\rm eq}$
Fe	4(j)	0.0000	0.3539(1)	0.5000	0.006(6)
Al	2(a)	0.0000	0.0000	0.0000	0.006(7)
B	4(i)	0.0000	0.2066(5)	0.0000	0.009(7)

where H_i, H_f are initial and final applied fields, and $T_2 - T_1$ is the change in temperature. For this formula to be valid, $T_2 - T_1$ should be small. Here $T_2 - T_1$ is taken to be 1 K. The entropy change calculation scheme in one complete cycle of magnetization and demagnetization is estimated in terms of the area between two consecutive isotherms between the given field limit as shown in Fig. 4(a). The measured entropy change as a function of temperature is presented in Fig. 4(b). The entropy change in 2 and 3 T applied fields is maximum around 276 K, being 3.78 and 4.87 J kg^{-1} K^{-1}, respectively. The 2 T applied-field entropy change data of this experiment agree very well with Ref. [9], shown as 2 T* data in Fig. 4(b). The entropy change values for our single crystalline samples are in close agreement with previously reported polycrystalline sample measured values as well [1,6].

Although $AlFe_2B_2$ is a rare-earth free material, its magnetocaloric property is larger than lighter rare-earth RT_2X_2 (R = rare earth, T = transition metal, and X = Si,Ge) compounds with $ThCr_2Si_2$-type structure (space group $I4/mmm$), namely $CeMn_2Ge_2$(∼1.8 J kg^{-1} K^{-1}) [24], $PrMn_2Ge_{0.8}Si_{1.2}$(∼1.0 J kg^{-1} K^{-1}) [25], and $Nd(Mn_{1-x}Fe_x)_2Ge_2$(∼ 1.0 J kg^{-1} K^{-1}) [26]. The entropy change of $AlFe_2B_2$ is significantly smaller than $Gd_5Si_2Ge_2$(∼ 13 J kg^{-1} K^{-1}); it has a comparable entropy change with elemental Gd(∼ 5.0 J kg^{-1} K^{-1}) [27]. These results show that $AlFe_2B_2$ has the potential to be used for magnetocaloric material considering the abundance of its constituents.

To precisely determine the Curie temperature, an Arrott plot was constructed using a wider range of $M(H)$ isotherms along the [100] direction [Fig. 3(d)]. In an Arrott plot, M^2 is plotted as a function of $\frac{H_{\rm int}}{M}$. $H_{\rm int} = H_{\rm app}$-$N^*M$ is the internal field inside the sample after the demagnetization field is subtracted. In this case, the experimental demagnetization factor along the easy axis of the sample was found to be almost negligible because of its thin, platelike shape, with the easy axis lying along the longest dimension of the sample. The details of determination of the experimental demagnetization factors and their comparison with theoretical data are explained in Refs. [23] and [28]. The Arrott plots have a positive slope indicating the transition is second-order [29]. In the mean-field approximation, in the limit of low fields, the Arrott isotherm corresponding to the Curie temperature is a straight line and passes through the origin. In Fig. 3(d), the isotherm corresponding to 276 K passes through the origin, but it is not a perfectly straight line. This suggests that the magnetic interaction in $AlFe_2B_2$ does not obey the mean-field theory. In the mean-field theory, electron correlation and spin fluctuations are neglected, but these can be significant around the transition temperature of an itinerant ferromagnet.

Since the Arrott plot data are not straight lines, a generalized Arrott plot is an alternative way to better confirm the Curie temperature. The generalized Arrott plot derived from the equation of state [30]

$$\left(\frac{H_{\rm int}}{M}\right)^{1/\gamma} = a\frac{T-T_C}{T} + bM^{1/\beta} \qquad (2)$$

is shown in Fig. 5. The critical exponents β and γ used in the equation of state are derived from the Kouvel-Fisher analysis

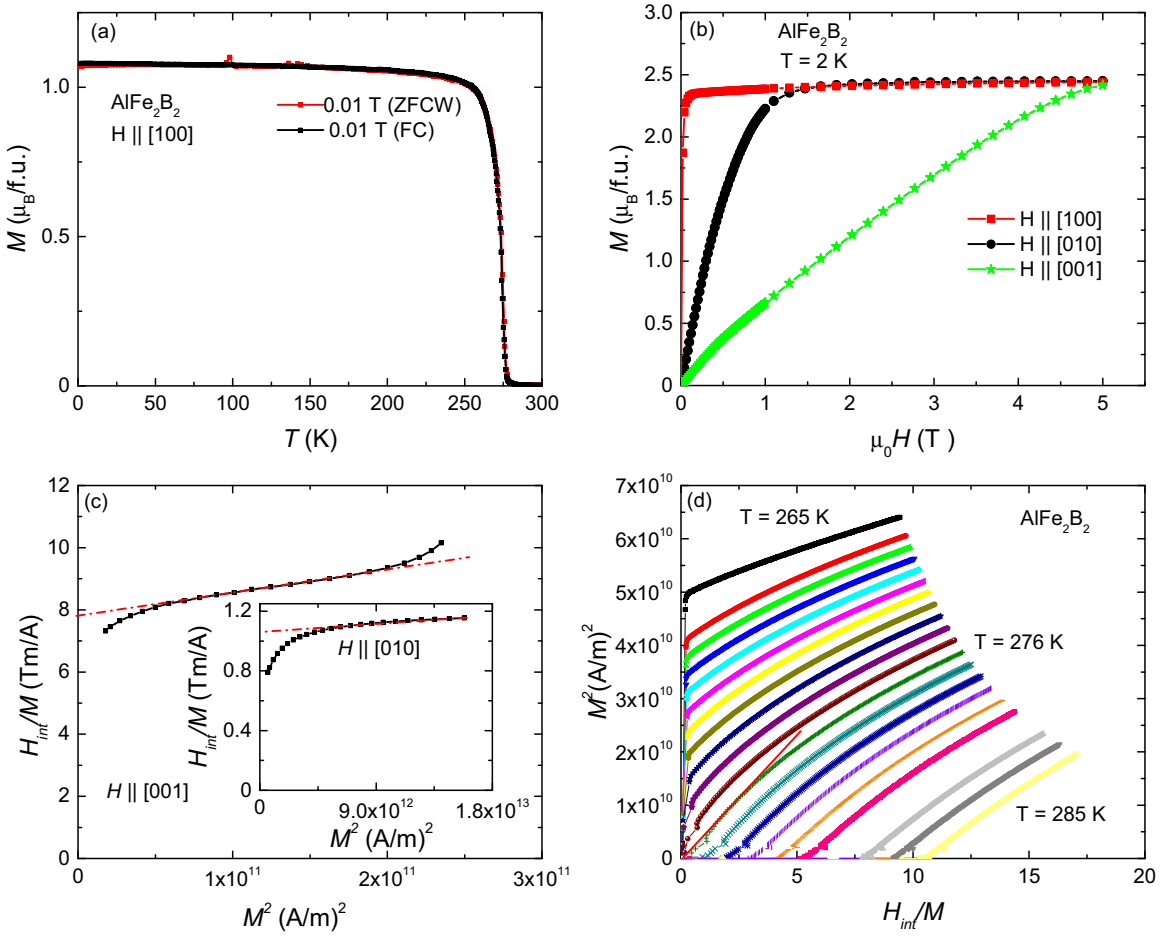

FIG. 3. (a) Temperature-dependent magnetization with a 0.01 T applied field along the [100] direction. (b) Field-dependent magnetization along principal directions at 2 K. [100] is the easy axis with the smallest saturating field, [010] is the intermediate axis with 1 T anisotropy, and [001] is the hardest axis with ∼5 T anisotropy field. (c) Sucksmith-Thompson plot for $M(H)$ data along the [001] direction (and along [010] in the inset) to estimate the magnetocrystalline anisotropy constants. The red dash-dotted line is the linear fit to the hard axes isotherms at the high-field region (> 3 T) whose Y intercept is used to estimate the anisotropy constant K. (d) Arrott plot obtained with easy-axis isotherms within the temperature range of 265–285 K at a step of 1 K. The straight line through the origin is the tangent to the isotherm corresponding to the transition temperature.

[31,32]. To determine β, the equation used was

$$M_S\left[\frac{d}{dT}(M_S)\right]^{-1} = \frac{T - T_C}{\beta}, \tag{3}$$

where the slope is $\frac{1}{\beta}$. The value of the spontaneous magnetization around the transition temperature was extracted from the Y intercept of M^4 versus $\frac{H}{M}$ [33], exploiting their straight line nature with a clear Y intercept. The experimental value of β was determined to be 0.30 ± 0.04, as shown in Fig. 6. The uncertainty in β was determined with fitting error as $\Delta\beta = \frac{\delta \text{slope}}{\text{slope}^2}$.

Similarly, the value of critical exponent γ was determined with the equation

$$\chi^{-1}\left[\frac{d}{dT}(\chi^{-1})\right]^{-1} = \frac{T - T_C}{\gamma}, \tag{4}$$

where the slope is $\frac{1}{\gamma}$, and $\chi^{-1}(T)$ is the initial high-temperature inverse susceptibility near the transition temperature. The experimental value of γ was determined to be 1.180 ± 0.005 as shown in Fig. 6.

Finally, the third critical exponent δ was determined using the equation

$$M \propto H^{1/\delta} \tag{5}$$

by plotting $\ln(M)$ versus $\ln(H)$ (Fig. 7) corresponding to Curie temperature 274 K. The experimental value of δ was determined by fitting $\ln(M)$ versus $\ln(H)$ over different ranges of applied field H. Taking the average of the range of δ value as shown in Fig. 7, we determine δ to be 4.9 ± 0.1, which was closely reproduced (4.93 ± 0.03) with Widom scaling theory $\delta = 1 + \frac{\gamma}{\beta}$.

Additionally, the validity of Widom scaling theory demands that the magnetization data should follow the scaling equation of the state. The scaling laws for a second-order magnetic phase transition relate the spontaneous magnetization $M_S(T)$ below T_C, the inverse initial susceptibility $\chi^{-1}(T)$ above T_C, and the magnetization at T_C with corresponding critical amplitudes by

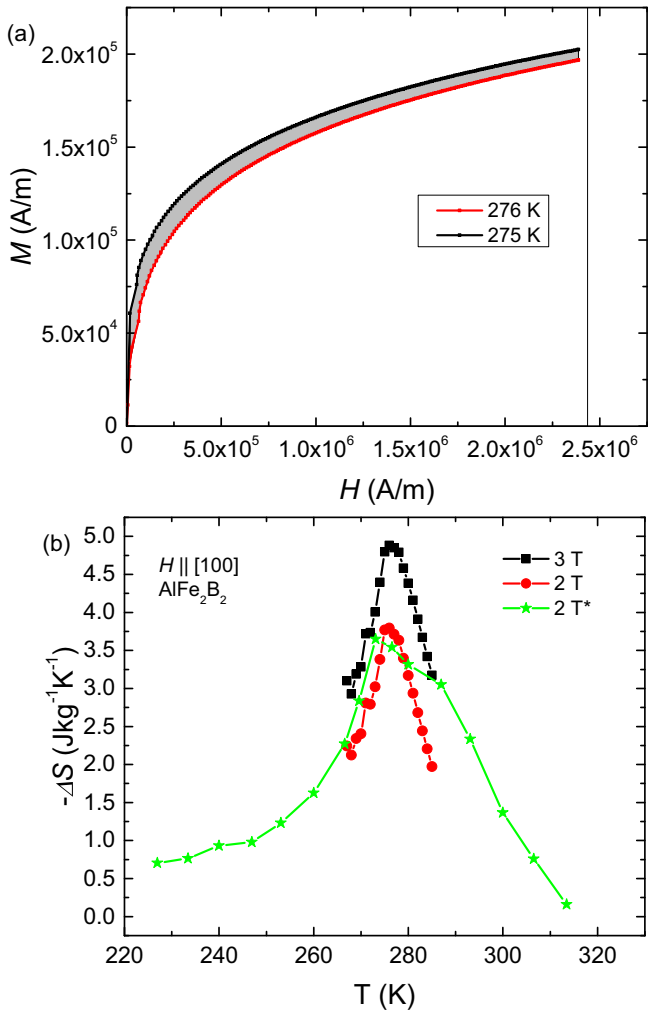

FIG. 4. Magnetocaloric effect in $AlFe_2B_2$ obtained using $M(H)$ isotherms along [100]. (a) The change in entropy (ΔS) evaluation scheme at its highest value, (b) the change in entropy with 2 T and 3 T applied fields using easy-axis [100] isotherms. For the sake of comparison, the 2 T* field data are taken from Ref. [9].

the following power laws:

$$M_S(T) = M_0(-\epsilon)^{\beta},\ \epsilon < 0, \tag{6}$$

$$\chi^{-1}(T) = \Gamma(\epsilon)^{\gamma},\ \epsilon > 0, \tag{7}$$

$$M = XH^{\frac{1}{\delta}}, \tag{8}$$

where M_0, Γ, and X are the critical amplitudes, and $\epsilon = \frac{T-T_C}{T_C}$ is the reduced temperature [34]. The scaling hypothesis assumes the homogeneous order parameter, which, with the scaling hypothesis, can be expressed as

$$M(H,\epsilon) = \epsilon^{\beta} f_{\pm}\left(\frac{H}{\epsilon^{\beta+\gamma}}\right), \tag{9}$$

where $f_+(T > T_C)$ and $f_-(T < T_C)$ are the regular functions. With new renormalized parameters, $m = \epsilon^{-\beta}M(H,\epsilon)$ and $h = \epsilon^{-(\beta+\gamma)}M(H,\epsilon)$, Eq. (9) can be written as

$$m = f_{\pm}(h). \tag{10}$$

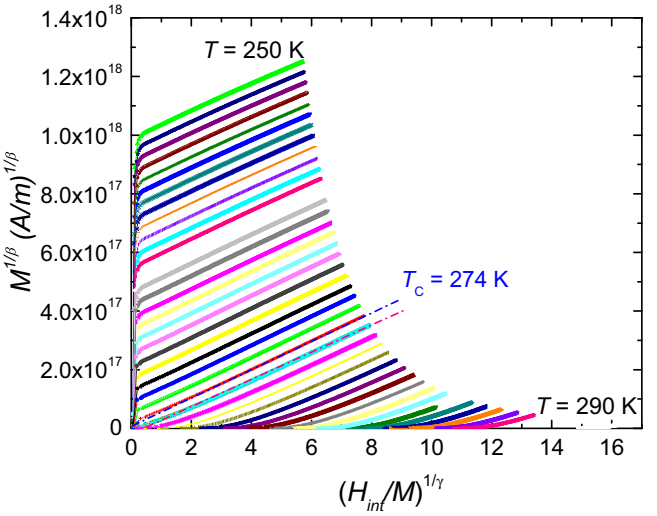

FIG. 5. Generalized Arrott plot of $AlFe_2B_2$ with magnetization data along the [100] direction within a temperature range of 250–290 K at a step of 1 K. $\beta = 0.30 \pm 0.04$ and $\gamma = 1.180 \pm 0.005$ were determined from the Kouvel-Fisher method. The two dash-dotted straight lines are drawn to visualize the intersection of the isotherms with the axes.

Up to linear order, the scaled m versus h graph is plotted as shown in Fig. 8 along with an inset in log-log scale, which clearly shows that all isotherms converge to two curves, one for $T > T_C$ and the other for $T < T_C$. This shows graphically that all the critical exponents were properly renormalized.

Finally, the consistency of the critical exponents β and γ is demonstrated [shown in Fig. 9(a)] by reproducing the initial spontaneous magnetization M_S and $\chi^{-1}(T)$ near the transition temperature using the Y and X intercepts of generalized Arrott plots as shown in Fig. 5, which overlaps with M_S obtained by M^4 versus $\frac{H}{M}$ [33] and initial inverse susceptibility $\chi^{-1}(T)$ with a 1 T applied field. The extracted data well fit [34] with corresponding power laws in Eqs. (6) and (7) as shown in Fig. 9(b) giving $\beta = 0.295 \pm 0.002$ and $\gamma = 1.210 \pm 0.003$, which closely agree with previously obtained K-F values.

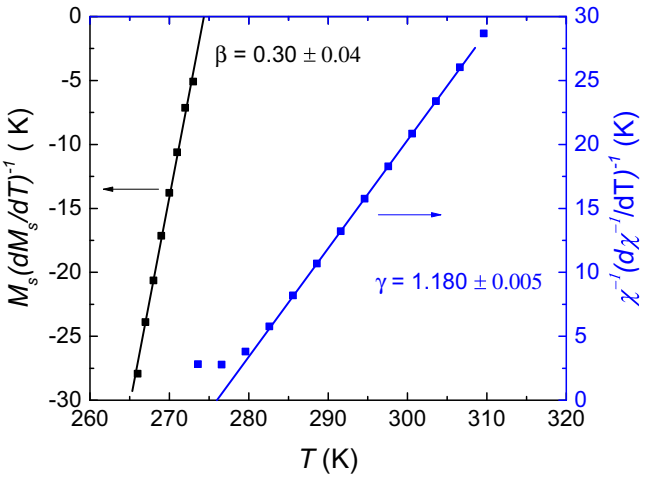

FIG. 6. Determination of the critical exponents (β and γ) using Kouvel-Fisher plots. See the text for details.

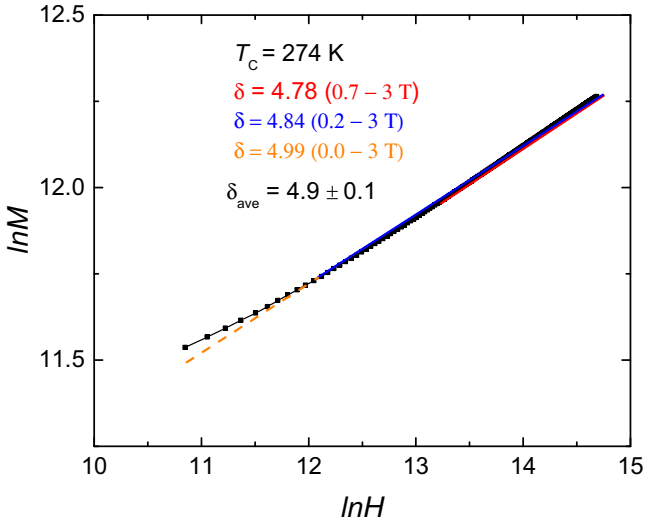

FIG. 7. Determination of the critical exponent δ using Kouvel-Fisher plots using an $M(H)$ isotherm at T_C to check the consistency of β and γ via Widom scaling. The data used for determining the exponent δ are highlighted with the red curve in the corresponding $M(H)$ isotherm. The data in the low-field region deviate slightly from the linear behavior in the logarithmic scale as shown in the inset. The range dependency of the value of δ is illustrated with different color tangents. The field range for the fitted data is indicated in the parentheses along with the value of δ. See the text for details.

The experimental values of the $AlFe_2B_2$ critical exponents ($\gamma = 1.18, \beta = 0.30, \delta = 4.93$) are comparable to those of the three-dimensional (3D) Ising model ($\gamma = 1.25$, $\beta = \frac{5}{16}$, $\delta = 5$) [35] and the 3D-XY model ($\gamma = 1.32, \beta = 0.35, \delta = 4.78$) [36] rather than those of the mean-field model ($\gamma = 1, \beta = 0.5$, $\delta = 3$). Further experimental and theoretical measurements

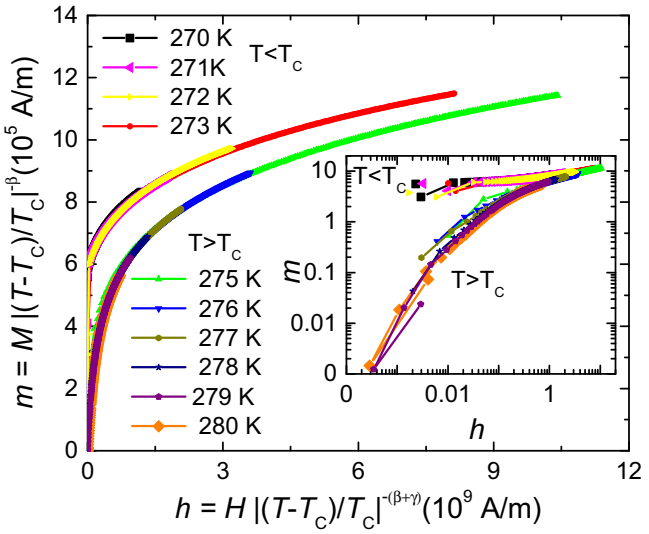

FIG. 8. Normalized isotherms to check the validity of the scaling hypothesis. The isotherms in between 270–273 K are converged to a higher value ($T < T_C$) and the isotherms in between 275–280 K are converged to a lower value ($T > T_C$). The inset shows the corresponding log-log plot clearly bifurcated in two branches in the low-field region.

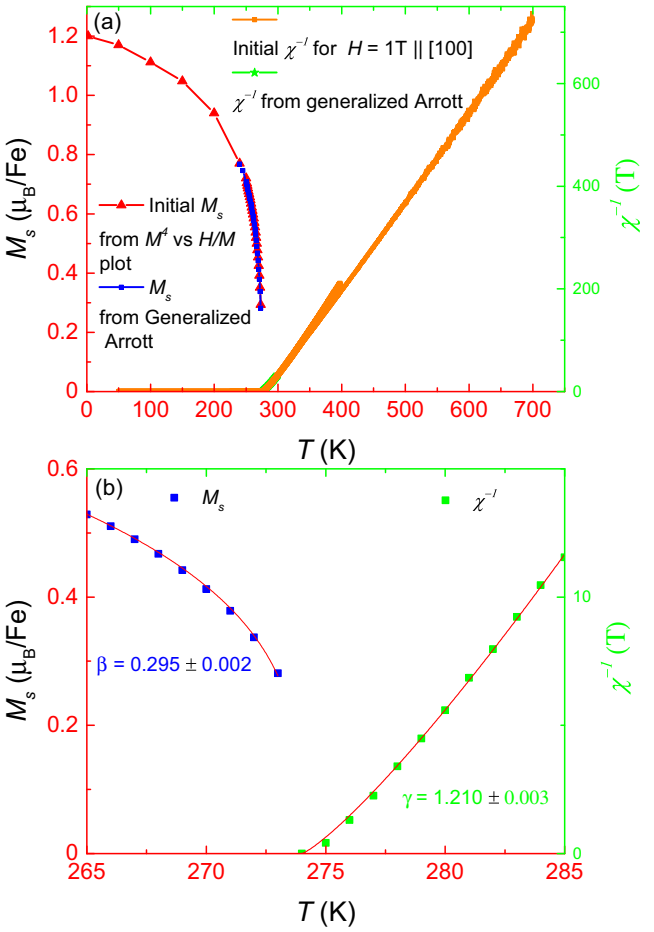

FIG. 9. Illustration of the consistency of the critical exponents β and γ used for the generalized Arrott plot (a) by reproducing the initial spontaneous magnetization M_S and $\chi^{-1}(T)$ via the Y and X intercepts of the generalized Arrott plot. (b) Fitting of the extracted data (squares) from the generalized Arrott plot with corresponding power laws (red lines) in Eqs. (6) and (7).

would be needed to further clarify the universality class of this material.

To measure the effective moment (μ_{eff}) of the Fe above the Curie temperature, a Curie-Weiss plot was prepared as shown in Fig. 9. The effective moment of the Fe ion above the Curie temperature was determined to be $2.15\mu_B$. Since the effective moment above the Curie temperature is almost equal to bcc Fe ($2.2\mu_B$) and the ordered moment at 2 K is significantly smaller than the Fe ion ($M_{\text{sat}} \sim 1.2\mu_B$/Fe) giving the low temperature Rhode-Wohlfarth ratio ($\frac{M_C}{M_{\text{sat}}}$) nearly equal to 1.14, where $\mu_{\text{eff}} = \sqrt{(8C)}$ and C is the Curie-Weiss constant given as $C = \frac{(\mu_B)^2}{3R} M_C(M_C + 2)$, this compound shows signs of an itinerant nature in its magnetization [37].

Itinerant magnetism, in general, can be tuned (meaning the size of the magnetic moment and the Curie temperature can be altered significantly and sometimes even suppressed completely) with an external parameter such as pressure or chemical doping. As a case study, we investigated the influence of external pressure on the ferromagnetism of $AlFe_2B_2$.

Figure 10 shows the pressure-dependent resistivity of single crystalline $AlFe_2B_2$ with current applied along the

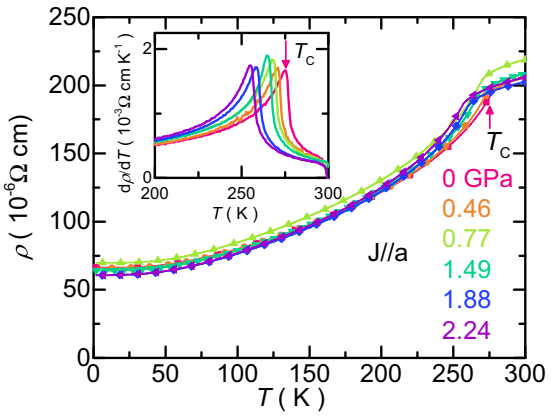

FIG. 10. Evolution of the single-crystal $AlFe_2B_2$ resistivity with hydrostatic pressure up to 2.24 GPa. Pressure values at T_C were estimated from linear interpolation between the $P_{300\,K}$ and $P_{T\leqslant 90\,K}$ values (see the text). Current was applied along the crystallographic a axis. The inset shows the evolution of the temperature derivative $d\rho/dT$ with hydrostatic pressure. The peak positions in the derivative were identified as transition temperature T_C. Examples of T_C are indicated by arrows in the figure.

crystallographic a axis. It shows metallic behavior with a residual resistivity of 60 $\mu\Omega$ cm. The metallic behavior was also predicted in density-functional calculation as well [38]. The ambient pressure temperature-dependent resistivity of $AlFe_2B_2$ shows a kink around 275 K, indicating a loss of spin disorder scattering associated with the onset of ferromagnetic order. As pressure is increased to 2.24 GPa, the temperature of this kink is steadily reduced. To determine the transition temperature T_C, the maximum in the temperature derivative $d\rho/dT$ is used, as shown in the inset of Fig. 10. The pressure dependence of T_C , i.e. the Curie-temperature - pressure phase diagram of $AlFe_2B_2$ is presented in Fig. 11. The transition temperature T_C is suppressed from 275 to 255 K when

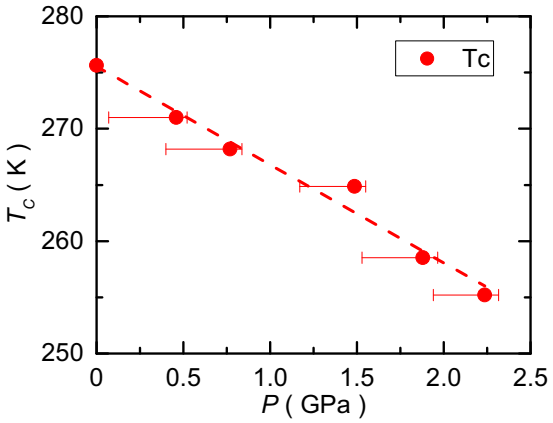

FIG. 11. Temperature-pressure phase diagram of $AlFe_2B_2$ as determined from resistivity measurement. Pressure values were estimated as being described in Fig. 10 and in the text. Error bars indicate the room-temperature pressure $P_{300\,K}$ and low-temperature pressure $P_{T\leqslant 90\,K}$. As shown in the figure, in the pressure region of 0–2.24 GPa the ferromagnetic transition temperature T_C is suppressed upon increasing pressure, with a suppressing rate around −8.9 K/GPa.

pressure is increased from 0 to 2.24 GPa, giving a suppression rate of −8.9 K/GPa. Interestingly, the Curie temperature suppression rate of $AlFe_2B_2$ is found to be comparable to the model itinerant magnetic materials such as helimagnetic MnSi (∼ − 15 K/GPa) [39] and weak ferromagnets $ZrZn_2$ (∼ − 13 K/GPa) [40] and Ni_3Al (∼ − 4 K/GPa) [41]. A linear fitting of the data as shown in Fig. 11 indicates that to completely suppress the T_C, around 31 GPa would be required. Usually such a linear extrapolation provides an upper estimate of the critical pressure.

V. FIRST-PRINCIPLES CALCULATIONS

Theoretical calculations for $AlFe_2B_2$ were performed using the all-electron density functional theory code WIEN2K [42–44]. The generalized gradient approximation according to Perdew, Burke, and Ernzerhof (PBE) [45] was used in our calculations. The sphere radii (RMT) were set to 2.21, 2.17, and 1.53 Bohr for Fe, Al, and B, respectively. RK_{max}, which defines the product of the smallest sphere radius and the largest plane-wave vector, was set to 7.0. All calculations were performed with the experimental lattice parameters as reported in Ref. [46] (which are consistent with our results) and all internal coordinates were relaxed until internal forces on atoms were less than 1 mRy/Bohr radius. All the calculations were performed in a collinear spin alignment. The magnetic anisotropy energy (MAE) was obtained by calculating the total energies of the system with spin-orbit coupling (SOC) with the magnetic moment along the three principal crystallographic axes. For these MAE calculations, the k-point convergence was carefully checked, and the calculations reported here were performed with 120,000 k points in the full Brillouin zone.

Similar to the experimental observation, $AlFe_2B_2$ is calculated to have ferromagnetic behavior, with a saturation magnetic moment (we do not include the small Fe orbital moment) of $1.36\mu_B$/Fe. This is in reasonable agreement with the experimentally measured value of $1.21\mu_B$/Fe. Interestingly this calculated magnetic moment on Fe is significantly lower than the moment on Fe in bcc Fe ($2.2\mu_B$/Fe), further suggesting a degree of itinerant behavior. The calculated density of states is shown in Fig. 12. As expected for a Fe-based ferromagnet, the electronic structure in the vicinity of the Fermi level is dominated by Fe d orbitals, and we observe a substantial exchange splitting of 2–3 eV.

For an orthorhombic crystal structure, the magnetic anisotropy energy is described by total energy calculations for the magnetic moments along each of the three principal axes [47]. For $AlFe_2B_2$, we find the [100] and [010] axes to be the "easy" directions, separated by just 0.016 meV per Fe, with [100] being the easiest axis. The [001] direction is the "hard" direction, which lies 0.213 meV per Fe above the [100] axis. As in our previous work on HfMnP [23], this value is much larger than the 0.06 meV value for hcp Co and likely results from a combination of the orthorhombic crystal structure and the structural complexity associated with a ternary compound. The 0.213 meV energy difference on a volumetric basis corresponds to an anisotropy constant K_1 as 1.48 MJ/m^3. (Note that we use the convention of the previous work and simply *define* K_1 for an orthorhombic system as the energy difference between the hardest and easiest

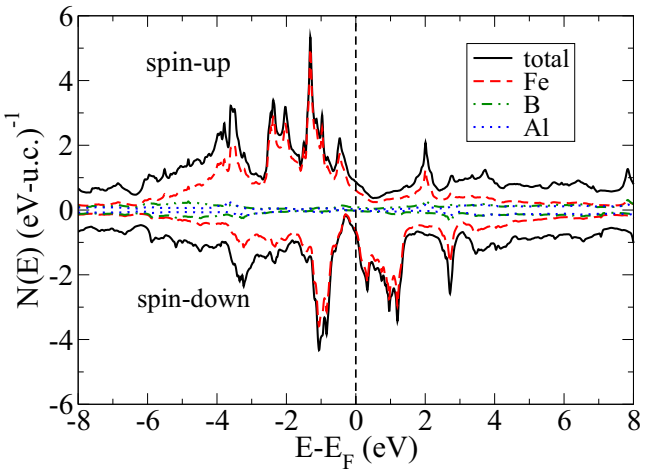

FIG. 12. The calculated density of states of $AlFe_2B_2$.

directions.) This magnetic anisotropy constant describes the energy cost associated with changing the orientation of the magnetic moments under the application of a magnetic field, and it is an essential component for permanent magnets. It is noteworthy that this anisotropy is comparable to the value of 2 MJ/m^3 proposed by Coey for an efficient permanent magnet [48], despite containing no heavy elements, using the approximation that $H_a \approx 2\mu_0 K_1/M_s$, with K as 1.48 MJ/m^3 and M_s as 0.68 T, yields an anisotropy field of 5.4 T, which is in excellent agreement with the experimentally measured value of 5 T and $K_{001} \approx 1.8$ MJ/m^3.

VI. CONCLUSIONS

Single crystalline $AlFe_2B_2$ was grown using the self-flux-growth technique and structural, magnetic, and transport properties were studied. $AlFe_2B_2$ is an orthorhombic, metallic ferromagnet with promising magnetocaloric behavior. The Curie temperature of $AlFe_2B_2$ was determined to be 274 K using the generalized Arrott plot method along with an estimation of critical exponents using Kouvel-Fisher analysis. The ordered magnetic moment (M_{sat}) at 2 K is $1.20\mu_B$/Fe which is much less than the paramagnetic Fe-ion moment at high temperature ($2.15\mu_B$/Fe), indicating itinerant magnetism. The magnetization in $AlFe_2B_2$ responds to the hydrostatic pressure with $\frac{dT_C}{dP} \sim -8.9$ K/GPa. A linear extrapolation of this $T_C(P)$ trend leads to an upper estimate of ~30 GPa required to fully suppress the transition. The saturation magnetization and anisotropic magnetic field predicted by first-principles calculations are in close agreement with the experimental results. The magnetocrystalline anisotropy fields were determined to be 1 T along the [010] direction and 5 T along the [001] direction with respect to easy-axis [100]. The magnetocrystalline anisotropy constants at 2 K are determined to be $K_{010} \approx 0.23$ MJ/m^3 and $K_{001} \approx 1.8$ MJ/m^3.

ACKNOWLEDGMENTS

We would like to thank W. R. McCallum and L. H. Lewis for drawing our attention to this compound, and A. Palasyuk for useful discussions. This research was supported by the Critical Materials Institute, an Energy Innovation Hub funded by the US Department of Energy, Office of Energy Efficiency and Renewable Energy, Advanced Manufacturing Office. This work was also supported by the office of Basic Energy Sciences, Materials Sciences Division, US DOE. L.X. was supported by the W. M. Keck Foundation. This work was performed at the Ames Laboratory, operated for DOE by Iowa State University under Contract No. DE-AC02-07CH11358.

[1] X. Tan, P. Chai, C. M. Thompson, and S. Michael, Magnetocaloric effect in $AlFe_2B_2$: Toward magnetic refrigerants from earth-abundant elements, J. Am. Chem. Soc. **135**, 9553 (2013).

[2] J. Cedervall, L. Häggström, T. Ericsson, and M. Sahlberg, Mössbauer study of the magnetocaloric compound $AlFe_2B_2$, Hyperfine Interact. **237**, 47 (2016).

[3] M. El Massalami, D. da S. Oliveira, and H. Takeya, On the ferromagnetism of $AlFe_2B_2$, J. Magn. Magn. Mater. **323**, 2133 (2011).

[4] W. Jeitschko, The crystal structure of Fe_2AlB_2, Acta Crystallogr. Sect. B **25**, 163 (1969).

[5] Y. B. Kuz'ma and N. F. Chaban, Crystal structure of the compound Fe_2AlB_2, Inorg. Mater. **5**, 321 (1969).

[6] Q. Du, G. Chen, W. Yang, J. Wei, M. Hua, H. Du, C. Wang, S. Liu, J. Han, Y. Zhang, and J. Yang, Magnetic frustration and magnetocaloric effect in $AlFe_{2-x}Mn_xB_2$($x = 0-0.5$) ribbons, J. Phys. D **48**, 335001 (2015).

[7] P. Chai, S. A. Stoian, X. Tan, P. A. Dube, and M. Shatruk, Investigation of magnetic properties and electronic structure of layered-structure borides AlT_2B_2 (T = Fe, Mn, Cr) and $AlFe_{2-x}Mn_xB_2$, J. Solid State Chem. **224**, 52 (2015), chemistry of two-dimensional materials.

[8] S. Hirt, F. Yuan, Y. Mozharivskyj, and H. Hillebrecht, $AlFe_{2-x}Co_xB_2$ ($x = 0$–0.30): T_C tuning through Co substitution for a promising magnetocaloric material realized by spark plasma sintering, Inorg. Chem. **55**, 9677 (2016).

[9] R. Barua, B. T. Lejeune, L. Ke, G. Hadjipanayis, E. M. Levin, R. W. McCallum, M. J. Kramer, and L. H. Lewis, Anisotropic magnetocaloric response in $AlFe_2B_2$, J. Alloys Compd. **745**, 505 (2018).

[10] Q. Du, G. Chen, W. Yang, Z. Song, M. Hua, H. Du, C. Wang, S. Liu, J. Han, Y. Zhang, and J. Yang, Magnetic properties of $AlFe_2B_2$ and $CeMn_2Si_2$ synthesized by melt spinning of stoichiometric compositions, Jpn. J. Appl. Phys. **54**, 053003 (2015).

[11] E. M. Levin, B. A. Jensen, R. Barua, B. Lejeune, A. Howard, R. W. McCallum, M. J. Kramer, and L. H. Lewis, Effects of Al content and annealing on the phases formation, lattice parameters, and magnetization of $Al_xFe_2B_2$ ($x = 1.0, 1.1, 1.2$) alloys, Phys. Rev. Mater. **2**, 034403 (2018).

[12] P. C. Canfield and Z. Fisk, Growth of single crystals from metallic fluxes, Philos. Mag. **65**, 1117 (1992).

[13] P. C. Canfield, T. Kong, U. S. Kaluarachchi, and N. H. Jo, Use of frit-disc crucibles for routine and exploratory solution growth of single crystalline samples, Philos. Mag. **96**, 84 (2016).

[14] S. L. Bud'ko, A. N. Voronovskii, A. G. Gapotchenko, and E. S. ltskevich, The fermi surface of cadmium at an electron-topological phase transition under pressure, J. Exp. Theor. Phys. **59**, 454 (1984).

[15] J. D. Thompson, Low-temperature pressure variations in a self-clamping pressure cell, Rev. Sci. Instrum. **55**, 231 (1984).

[16] M. S. Torikachvili, S. K. Kim, E. Colombier, S. L. Bud'ko, and P. C. Canfield, Solidification and loss of hydrostaticity in liquid media used for pressure measurements, Rev. Sci. Instrum. **86**, 123904 (2015).

[17] A. Eiling and J. S. Schilling, Pressure and temperature dependence of electrical resistivity of Pb and Sn from 1-300K and 0-10 GPa-use as continuous resistive pressure monitor accurate over wide temperature range; superconductivity under pressure in Pb, Sn and In, J. Phys. F **11**, 623 (1981).

[18] B. Bireckoven and J. Wittig, A diamond anvil cell for the investigation of superconductivity under pressures of up to 50 GPa: Pb as a low temperature manometer, J. Phys. E **21**, 841 (1988).

[19] S. K. Kim, M. S. Torikachvili, E. Colombier, A. Thaler, S. L. Bud'ko, and P. C. Canfield, Combined effects of pressure and Ru substitution on $BaFe_2As_2$, Phys. Rev. B **84**, 134525 (2011).

[20] SHELXTL-v2008/4, Bruker AXS Inc., Madison, WI, 2013.

[21] B. H. Toby, *EXPGUI*, a graphical user interface for *GSAS*, J. Appl. Crystallogr. **34**, 210 (2001).

[22] W. Sucksmith and J. E. Thompson, The magnetic anisotropy of cobalt, Proc. R. Soc. London, Ser. A **225**, 362 (1954).

[23] T. N. Lamichhane, V. Taufour, M. W. Masters, D. S. Parker, U. S. Kaluarachchi, S. Thimmaiah, S. L. Bud'ko, and P. C. Canfield, Discovery of ferromagnetism with large magnetic anisotropy in ZrMnP and HfMnP, Appl. Phys. Lett. **109**, 092402 (2016).

[24] M. F. Md Din, J. L. Wang, Z. X. Cheng, S. X. Dou, S. J. Kennedy, M. Avdeev, and S. J. Campbell, Tuneable magnetic phase transitions in layered $CeMn_2Ge_{2-x}Si_x$ compounds, Sci. Rep. **5**, 11288 (2015).

[25] J. L. Wang, S. J. Campbell, R. Zeng, C. K. Poh, S. X. Dou, and S. J. Kennedy, Re-entrant ferromagnet $PrMn_2Ge_{0.8}Si_{1.2}$: Magnetocaloric effect, J. Appl. Phys. **105**, 07A909 (2009).

[26] Y. Q. Chen, J. Luo, J. K. Liang, J. B. Li, and G. H. Rao, Magnetic properties and magnetocaloric effect of $Nd(Mn_{1-x}Fe_x)_2Ge_2$ compounds, J. Alloys Compd. **489**, 13 (2010).

[27] V. K. Pecharsky and K. A. Gschneidner, Jr., Giant Magnetocaloric Effect in $Gd_5(Si_2Ge_2)$, Phys. Rev. Lett. **78**, 4494 (1997).

[28] T. N. Lamichhane, V. Taufour, S. Thimmaiah, D. S. Parker, S. L. Bud'ko, and P. C. Canfield, A study of the physical properties of single crystalline Fe_5B_2P, J. Magn. Magn. Mater. **401**, 525 (2016).

[29] B. K. Banerjee, On a generalised approach to first and second order magnetic transitions, Phys. Lett. **12**, 16 (1964).

[30] A. Arrott and J. E. Noakes, Approximate Equation of State for Nickel Near its Critical Temperature, Phys. Rev. Lett. **19**, 786 (1967).

[31] J. S. Kouvel and M. E. Fisher, Detailed magnetic behavior of nickel near its Curie point, Phys. Rev. **136**, A1626 (1964).

[32] Ch. V. Mohan, M. Seeger, H. Kronmüller, P. Murugaraj, and J. Maier, Critical behavior near the ferromagnetic-paramagnetic phase transition in $La_{0.8}Sr_{0.2}MnO_3$, J. Magn. Magn. Mater **183**, 348 (1998).

[33] B. Chen, J. H. Yang, H. D. Wang, M. Imai, H. Ohta, C. Michioka, K. Yoshimura, and M. H. Fang, Magnetic properties of layered itinerant electron ferromagnet Fe_3GeTe_2, J. Phys. Soc. Jpn. **82**, 124711 (2013).

[34] A. K. Pramanik and A. Banerjee, Critical behavior at paramagnetic to ferromagnetic phase transition in $Pr_{0.5}Sr_{0.5}MnO_3$: A bulk magnetization study, Phys. Rev. B **79**, 214426 (2009).

[35] D. S. Gaunt, The critical isotherm and critical exponents of the three-dimensional Ising ferromagnet, Proc. Phys. Soc. **92**, 150 (1967).

[36] M. Campostrini, M. Hasenbusch, A. Pelissetto, P. Rossi, and E. Vicari, Critical behavior of the three-dimensional XY universality class, Phys. Rev. B **63**, 214503 (2001).

[37] P. Rhodes and E. P. Wohlfarth, The effective Curie-Weiss constant of ferromagnetic metals and alloys, Proc. R. Soc. London A **273**, 247 (1963).

[38] Y. Cheng, Z. L. Lv, X. R. Chen, and L. C. Cai, Structural, electronic and elastic properties of $AlFe_2B_2$: First-principles study, Comput. Mater. Sci. **92**, 253 (2014).

[39] C. Pfleiderer, D. Reznik, L. Pintschovius, H. v. Löhneysen, M. Garst, and A. Rosch, Partial order in the non-Fermi-liquid phase of MnSi, Nature (London) **427**, 227 (2004).

[40] M. Uhlarz, C. Pfleiderer, and S. M. Hayden, Quantum Phase Transitions in the Itinerant Ferromagnet $ZrZn_2$, Phys. Rev. Lett. **93**, 256404 (2004).

[41] P. G. Niklowitz, F. Beckers, G. G. Lonzarich, G. Knebel, B. Salce, J. Thomasson, N. Bernhoeft, D. Braithwaite, and J. Flouquet, Spin-fluctuation-dominated electrical transport of Ni_3Al at high pressure, Phys. Rev. B **72**, 024424 (2005).

[42] P. Blaha, K. Schwarz, G. K. H. Madsen, D. Kvasnicka, and J. Luitz, *WIEN2K, An Augmented Plane Wave + Local Orbitals Program for Calculating Crystal Properties* (Karlheinz Schwarz, Techn. Universität Wien, Austria, 2001).

[43] E. Sjostedt, L. Nordstrom, and D. J. Singh, An alternative way of linearizing the augmented plane-wave method, Solid State Commun. **114**, 15 (2000).

[44] D. J. Singh and L. Nordstrom, *Planewaves Pseudopotentials and the LAPW Method*, 2nd ed. (Springer, Berlin, 2006).

[45] J. P. Perdew, K. Burke, and M. Ernzerhof, Generalized Gradient Approximation Made Simple, Phys. Rev. Lett. **77**, 3865 (1996).

[46] J. Cedervall, M. S. Andersson, T. Sarkar, E. K. Delczeg-Czirjak, L. Bergqvist, T. C. Hansen, P. Beran, P. Nordblad, and M. Sahlberg, Magnetic structure of the magnetocaloric compound $AlFe_2B_2$, J. Alloys Compd. **664**, 784 (2016).

[47] W. Palmer, Magnetocrystalline anisotropy of magnetite at low temperature, Phys. Rev. **131**, 1057 (1963).

[48] J. M. D. Coey, Hard magnetic materials: A perspective, IEEE Trans. Magn. **47**, 4671 (2011).